

Reverse strain-induced snake states in graphene nanoribbons

Cheng-yi Zuo,¹ Junjie Qi,² Tian-lun Lu,¹ Zhi-qiang Bao,^{3,*} and Yan Li^{1,†}

¹Department of Physics, State Key Laboratory of Precision Spectroscopy, School of Physics and Electronic Science, East China Normal University, Shanghai 200241, China

²Beijing Academy of Quantum Information Sciences, West Bld.3, No.10 Xibeiwang East Rd., Haidian District, Beijing 100193, China

³Key Laboratory of Polar Materials and Devices (MOE), Department of Electronics, East China Normal University, Shanghai 200241, China

Strain can tailor the band structures and properties of graphene nanoribbons (GNRs) with the well-known emergent pseudo-magnetic fields and the corresponding pseudo-Landau levels (pLLs). We design one type of the zigzag GNR (ZGNR) with reverse strains, producing pseudo-magnetic fields with opposite signs in the lower and upper half planes. Therefore, electrons propagate along the interface as “snake states”, experiencing opposite Lorentz forces as they cross the zero field border line. By using the Landauer-Büttiker formalism combined with the nonequilibrium Green’s function method, the existence and robustness of the reverse strain-induced snake states are further studied. Furthermore, the realization of long-thought pure valley currents in monolayer graphene systems is also proposed in our device.

I. INTRODUCTION

Graphene, a single-atom-layer carbon material, has the peculiar band structure with two nonequivalent Dirac points K and K' , leading to a pseudo-spin degree of freedom, i.e., valley [1–3]. The field utilizing the valley degree of freedom is referred to as valleytronics [4], which takes advantage of graphene and gapped 2 dimensional (2D) Dirac materials [5–8]. Graphene nanoribbons (GNRs), cut from the graphene, are quasi-one-dimensional systems. There are two basic shapes for GNR edges — zigzag and armchair edges, and more specially, the zigzag GNRs (ZGNRs) support zero-energy flat bands of edge states [9–13]. In our work, we mainly focus on the ZGNRs. Straintronics, a new discipline developed in recent decades, utilizes strain engineering methods and strain-induced physical effects to develop novel functional devices [14–19]. Because graphene has the outstanding capability to sustain nondestructive reversible deformations up to high values 25% to 27% [20–23], it can be a good candidate for making novel strain devices [24]. One of the most remarkable properties induced by the strain in graphene is the appearance of the pseudo-magnetic fields and the corresponding pseudo-Landau level (pLLs) [25–33], which have been observed in several excellent experiments [34–39].

Previous work usually considers the model shown in Fig. 1(a) [29, 36, 40], where the ZGNR is stretched along the y direction, and assuming the hopping coefficients are constant along the x direction but decreasing successively from the lower edge to the upper one. Obviously, stretching increases the bond lengths, thus it will decrease the hopping coefficients which depend on the overlap integral of wave functions belonging to neighbouring sites. As a

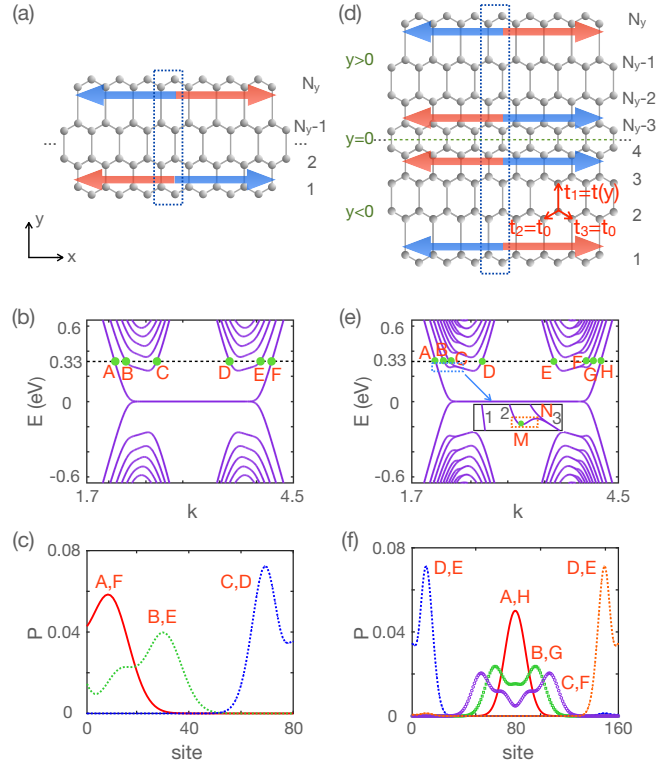


FIG. 1. (a) and (d) are the schematic diagrams of the ZGNR with MIS and SS, respectively. The blue dotted rectangle represents a primitive cell for the ZGNR, and the red (blue) arrows depict the current for K (K') valley. (b) and (c) ((e) and (f)) are energy bands and the distributions of wave functions for the ZGNR with MIS (SS).

result, we call this strain pattern the monotone increasing strain (MIS), and if the hopping coefficients decrease linearly, a uniform perpendicular pseudo-magnetic field emerges and acts on the electrons locally, leading to the specific dispersive pLLs [29, 40]. Until now, the MIS

* zqbao@phy.ecnu.edu.cn

† yli@phy.ecnu.edu.cn

configuration in GNRs has been well-studied and can be realized by various methods [31, 41]. Even though the ZGNRs with MIS are charming, we suppose that another strain pattern shown in Fig. 1(d) may be easier to realize. It is clearly that the ZGNR with symmetrical structures in Fig. 1(d) can be viewed as two copies of the ZGNR in Fig. 1(a) where the lower copy ($y < 0$) is the horizontal inversion partner of the upper copy ($y > 0$). The corresponding strain pattern we named the symmetrical strain (SS). It should be pointed out that even though we call it SS and the structure in Fig. 1(d) respects the inversion symmetry, the accurate symmetry between the lower and upper planes is not necessary. To be precise, what we need are the reverse strains between the lower and half planes, and without loss of generality, we use the SS to simplify our discussions. We can expect that the ZGNR with SS may be more natural to fabricate in the suspended devices [42–44]. Simply speaking, if the ZGNR is stretched along the y direction, and the $n_y = 1$ and $n_y = N_y$ edges are fixed by probes or substrates, the SS pattern maybe form naturally. In Ref. [42], a single graphene layer is placed over an array of pits etched in SiO₂/Si substrate. Continuously deformation can be tuned in this suspended device, producing regions with opposite signs of the pseudo-magnetic fields. In fact, what we need is the device naturally allowing for pseudo-magnetic fields changing sign, which occurs at the center of the ZGNR with reverse strains.

Polarized valley currents are predicted in the ZGNR with MIS [40], so the meaningful question is what form should the valley currents present in the ZGNR with SS. Interestingly we found that except for the states propagating along the edges, emergent snake states can flow in the middle of the sample, which constitutes a new type of quantum valley Hall effect (QVHE). Even though this kind of snake states may be viewed as the bound states near the domain wall — 1D “line defect” along the $y = 0$ line — between the lower and upper half parts, they are still fascinating because: (i) this 1D “line defect” is natural and “invisible”, and we don’t need to dope any real impurities; (ii) the reverse strain-induced snake states come from a fascinating phenomenon — the pseudo-magnetic fields have opposite directions between the lower and upper half parts, which is the result of the SS.

The paper is organized as follows. In Sec. II, we show the formation mechanism of the reverse strain-induced snake states. In Sec. III, we propose that the pure valley currents exist in the ZGNR with SS, which can be measured through the charge transport. In Sec. IV, we verify the existence of the snake states by the conductance of the two-terminal device calculated by the Landauer-Büttiker formalism and nonequilibrium Green’s function method, and discuss the robustness of the snake states. Sec. V is the conclusion.

II. THE APPEARANCE OF THE REVERSE STRAIN-INDUCED SNAKE STATES

The Hamiltonian in the tight-binding representation of the strained ZGNRs is $\mathcal{H} = \sum_i \varepsilon_i a_i^\dagger a_i - \sum_{\langle ij \rangle} t a_i^\dagger a_j$, where ε_i is the onsite energy, a_i^\dagger and a_i represent the creation and annihilation operators. For simplicity, we only consider the nearest-neighbor hopping, neglecting the next-nearest-neighbor hopping [40]. The strain pattern is contained in the hopping coefficient t . Since the strain is along the y direction, we assume that the hopping coefficients along the x direction, such as t_2 and t_3 in Fig. 1(d) are constant and set as the well-known hopping coefficient for the normal graphene $t_0 = -2.75$ eV [45]. In the y direction, the hopping coefficient $t(y)$ is dependent on the coordinate y and we suppose that it is a linear function of y in both upper and lower half planes. Because we assume that the positions of both edges ($n_y = 1$ and $n_y = N_y$) are fixed, which can be realized in the suspended graphene, the SS configuration could be formed. In this situation, the strength of deformation is minimum (maximum) in the middle (edge) position. For simplicity, we suppose $t(y)$ is t_0 and $t_0(1 - \eta)$ in the middle and edge position, respectively, where η is an adjustable variable which reflects the strain strength. In the following calculations, we take $\eta = 0.5$, which can be achieved in the experiments. First, we know that the graphene can sustain nondestructive reversible deformations up to high values 25% to 27% [20–23]. Second, previous work has presented this relation $t_y = t_0 \exp[-\beta(\ell/a_0 - 1)]$ [23], where ℓ is the carbon-carbon distance, $a_0 = 0.142$ nm is the equilibrium distance between neighboring carbon atoms, and $\beta \approx 3.37$ is the decay rate. As a result, if we take $\ell = 1.25a_0$ for the deformation value 25%, we will get $t_y \approx 0.43t_0$, which suggests that the strain strength $\eta = 0.5$ falls in the nondestructive reversible region.

Fig. 1(b) shows the band structure of the ZGNR with MIS in Fig. 1(a) with $N_y = 80$ and $\eta = 0.5$. In our calculations, the hopping coefficients are supposed to be constant along the x direction and to linearly decrease along the y direction [30]. As a result, the difference of t_y between neighboring carbon atoms along the y direction is approximately 0.6%. It is clearly that the dispersive pseudo-Landau levels form in the low energy regime, which is consistent with Ref. [30, 40]. In order to explore the probability distributions of the wave functions belonging to each band, we analysis the situations for selected k points. Typical results are demonstrated in Fig 1(c), where we have chosen the k points A-F at the intersections of the energy line $E = 0.33$ eV and the lowest energy bands in Fig. 1(b). It is clearly shown that the wave functions associated with points A and C distribute near the lower and upper edges, respectively. As a comparison, the wave function of point B spreads into the bulk. We have checked that the wave functions of adjacent k points near A, B, C have the similar localized properties with them. Additionally, the band structures and wave functions associated with D, E, F are the same

with that of C, B and A, which is shown in Figs. 1(b) and (c).

Fig. 1(e) shows the band structure of the ZGNR with SS in Fig. 1(d) with $N_y = 160$ and $\eta = 0.5$. The pseudo-magnetic field induced by the strain is about 49T, which is estimated in Appendix A. The most difference between the ZGNR with SS and the one with MIS is the former possesses reverse strains between the lower and half planes, which provides the possibility for the snake states discussed below. Similar to Fig. 1(b), the k points A-H at the intersections of the energy line $E = 0.33$ eV and the lowest energy bands are chosen in Fig. 1(e). Combined with the results in Fig. 1(f), we can see that the wave functions associated with points A and H (D and E) moves to the middle position (new edges). This result can be easily understood since the wave functions associated with point A (C) distribute near the lower (upper) edge which holds no strain strength (the max strain strength). In the ZGNR with SS in Fig. 1(d), the distributions follow the same rule, i.e., the wave functions associated with points A and H (D and E) distribute around the positions with no strain strength (the max strain strength). Similarly, the wave function associated with points B, G, C and F spreads into the bulk. In addition, from the partial enlarged diagram in Fig. 1(e) we can see that, the first pLL splits into band 2 and band 3 at point N due to the boundary condition [46]. Accordingly, a minimal point M emerge, and the surround band in the orange dotted rectangle will contribute additional edge states when the Fermi level across.

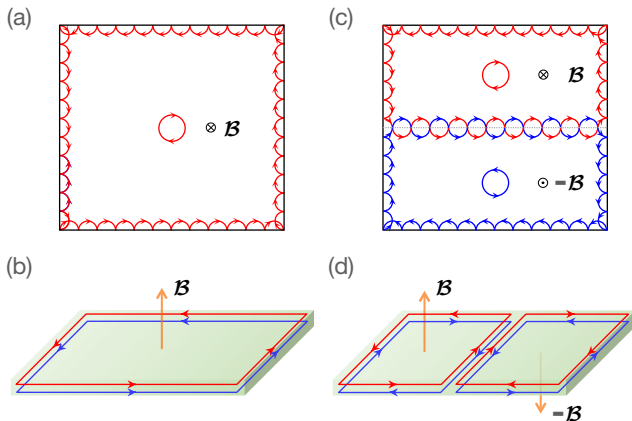


FIG. 2. (a) and (b) show the QH edge states, where the electrons take circular motions under the perpendicular magnetic field. (c) and (d) show the QVH edge states, where the electrons take circular motions under the perpendicular pseudo-magnetic fields. Because the electrons experience opposite Lorentz forces as they cross the zero field border line, the snake states propagate along the interface.

It should be pointed out that the two valleys K and K' are decoupled in the low-energy limit making the study on the valley transport meaningful, as long as no scattering terms can connect the two valleys. As a result, if the Fermi energy lies between adjacent pLLs, the edge states

with valley degree of freedom will dominate the transport. We compare the difference between edge states in our model and that in the normal quantum Hall (QH) states in Fig. 2. The key point is that the directions of the pseudo-magnetic fields, as well as the reverse strains, are opposite between the lower ($y < 0$) and upper ($y > 0$) half planes. As a result, the electrons experience opposite Lorentz forces as they cross the zero field border line, resulting in the emergence of the snake states [47–50] in the middle of the sample. In our setup, the snake states and the edge states co-participate the circular flow in both half planes, leading to the new type of QVH effect, which can be viewed as two copies of conventional QVH states.

III. PURE VALLEY CURRENTS

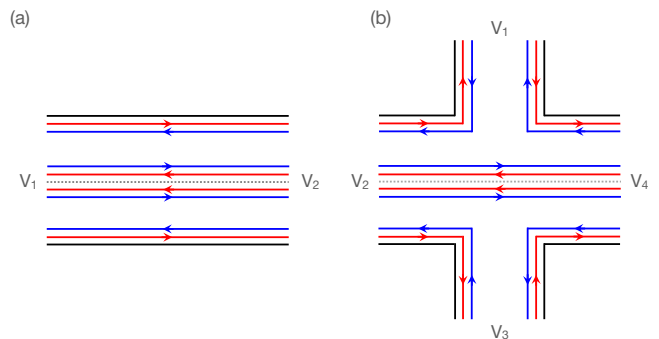


FIG. 3. Schematic diagram showing (a) two-terminal and (b) four-terminal measurement geometries. In (a) a charge current $I^c = 4e^2V/h$ flows into the right lead. In (b) a valley current $I^v = e^2V/h$ flows into the right lead.

The generation of pure valley currents has attracted lots of attention in the past few years. Several theoretical schemes, e.g., optical excitations [51], quantum pumping [52, 53], cyclic strain deformations [54], and applying AC bias [55], have been proposed for realizing pure valley currents. In the laboratory, pure valley currents also have been observed in graphene superlattice [56] and graphene bilayers [57–59]. However, pure valley currents are very difficult to be observed in the monolayer graphene [40, 60].

Using similar methods in Ref. [61] in which pure spin currents are discussed, we use the Landauer-Büttiker formula to discuss the valley currents in two and four terminal devices shown in Fig. 3. Different from the usual QH and quantum spin Hall effect (QSHE) where the 1D conducting states localizing in the edges, the snake states exist in our device and contribute to transport. According to the Büttiker formula [62], the current in i -th terminal in the equilibrium is

$$I_i^\sigma = \frac{e^2}{h} \sum_{j \neq i} (T_{ji}^\sigma V_i - T_{ij}^\sigma V_j), \quad (1)$$

where V_i is the voltage in the i -th terminal and T_{ij}^σ is the transmission coefficient for valley σ ($\sigma = K, K'$) current between the i -th and j -th terminals. Naturally, the charge current and valley current can be defined by $I_i^c = I_i^K + I_i^{K'}$ and $I_i^v = I_i^K - I_i^{K'}$.

For the two-terminal device shown in Fig. 3(a), $T_{12}^\sigma = T_{21}^\sigma = 2$, thus we get $I_2^K = (2V_1 - 2V_2)e^2/h$ and $I_2^{K'} = (2V_1 + 2V_2)e^2/h$ for terminal 2. If we take $V_1 = V/2$ and $V_2 = -V/2$, then $I_2^K = 2e^2V/h$, $I_2^{K'} = 2e^2V/h$. As a result, $I_2^c = 4e^2V/h$, $I_2^v = 0$. This suggests that the pure valley currents cannot exist in the two-terminal device. Next we study the four-terminal device shown in Fig. 3(b) to see whether the pure valley currents can survive. In this case, the transmission coefficients for K valley currents are $T_{14}^K = T_{21}^K = T_{23}^K = T_{34}^K = 1$, $T_{42}^K = 2$ and 0 otherwise; the transmission coefficients for K' valley currents are $T_{12}^{K'} = T_{32}^{K'} = T_{41}^{K'} = T_{43}^{K'} = 1$, $T_{24}^{K'} = 2$ and 0 otherwise. Therefore, we can get $I_4^c = (V_1 + 2V_2 + V_3 - 4V_4)e^2/h$ and $I_4^v = (-V_1 + 2V_2 - V_3)e^2/h$. If we take $V_1 = -V/2$, $V_2 = V/4$, $V_3 = V_4 = 0$, we have $I_4^c = 0$ but $I_4^v = e^2V/h$, which suggest that we can obtain the pure valley currents in terminal 4. In other words, the pure valley currents can be measured through the charge transport in a mesoscopic system as shown in Fig. 3. It should be pointed out that this is one simple and elegant way to realize the pure valley currents in the monolayer graphene systems.

IV. CONDUCTANCES FROM THE EDGE STATES AND SNAKE STATES

Next we use the nonequilibrium Green's function method to calculate the conductance of the strained ZGNR shown in Fig. 4(a), where L and R denote the left and right semi-infinite long leads, and C represents the central part with the width $N_y = 160$ and length $N_x = 60$ (60 primitive cells in the x direction). It should be pointed out that the central part and the leads are all stretched along the transverse direction, thus the snake states could survive in the whole system. Since our calculations based on the tight binding model, the central part and two leads are all described by the Hamiltonian $\mathcal{H} = \sum_i \varepsilon_i a_i^\dagger a_i - \sum_{\langle ij \rangle} t a_i^\dagger a_j$, even though each part may possess different onsite energies ε_i . The linear conductance of the strained ZGNR is $G = \lim_{V \rightarrow 0} dI/dV$, where the current I is obtained by the Landauer-Büttiker formula [45, 63]: $I = (2e/h) \int d\varepsilon T_{LR}(\varepsilon) [f_L(\varepsilon) - f_R(\varepsilon)]$. Here $f_\alpha = 1/\{\exp[(\varepsilon - eV_\alpha)/k_B T] + 1\}$ is the Fermi function of the α ($\alpha = L, R$) lead, and $T_{LR}(\varepsilon) = \text{Tr}(\Gamma_L \mathbf{G}^r \Gamma_R \mathbf{G}^a)$ is the transmission coefficient with the linewidth functions $\Gamma_\alpha = i[\Sigma_\alpha^r(\varepsilon) - \Sigma_\alpha^a(\varepsilon)]$ and the self-energy $\Sigma_\alpha^{r/a}$. The retarded and advanced Green's func-

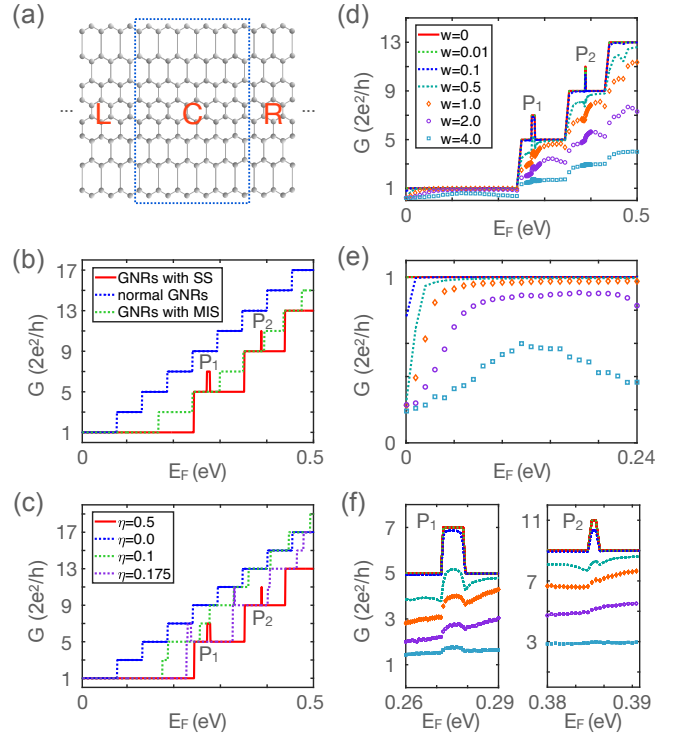


FIG. 4. Conductances versus Fermi energy for the strained ZGNRs. (a) is the schematic diagram of the two-terminal device. (b) shows the conductance plateaus for the ZGNR without strain, ZGNR with SS and ZGNR with MIS, respectively. (c) illustrates the conductances of the ZGNR with SS for different strain strength. (d)-(f) show the influences of Anderson disorders on conductances with (e) and (f) from (d).

tion is $\mathbf{G}^r(\varepsilon) = 1/[\varepsilon - \mathbf{H}_{cen} - \Sigma_L^r - \Sigma_R^r]$ and $\mathbf{G}^a(\varepsilon) = [\mathbf{G}^r(\varepsilon)]^\dagger$, respectively, where \mathbf{H}_{cen} is the Hamiltonian of the central region. In the following numerical calculations, we take the hopping energy $t_0 \approx 2.75$ eV, and since the t_0 corresponds to 10^4 K, we can safely set the temperature to zero in our calculations [45].

We first study the clean strained ZGNRs. Fig. 4(b) compares three strain patterns: the blue dash-dot line shows the conductance without strain, which is quantized and exhibits a series of equidistant plateaus due to the transverse sub-bands of the ZGNR with finite width. The green dot line corresponds to the conductance of the ZGNR with MIS. It is clear that due to the formation of the pLLs, the width of the lower plateaus increases. Furthermore, the step interval of the plateaus maintains $4e^2/h$ which is attributed to the states located in the two edges. After we introduce the SS, the step interval of the plateaus increases to $8e^2/h$, which implies the formation of the snake states in the middle of the sample. It should be pointed out that two peaks P_1 and P_2 emerge on the second and third plateaus due to the energy bands inside the orange dot rectangle in Fig. 1(e). More discussions on P_1 and P_2 can be found in Appendix B. In fact, P_1

and P_2 are two narrow plateaus which is clearly shown in Fig. 4(f). From Fig. 1(e) we can see that the points similar with the emergent minimum point N are more difficult to appear on higher pLLs, thus the strengths of the similar narrow plateaus become smaller with increasing E_F .

In fact, the strain strength plays the role of the pseudo-magnetic fields, contributing to the pLLs and the quantized valley Hall conductance. Therefore, we plot Fig. 4(c) to illustrate the conductance with the change in strain, which shows the evolution of step interval from $4e^2/h$ to $8e^2/h$. Blue dot line corresponds to the ZGNR without strain, and according to the above analysis, the step interval is $4e^2/h$. The green dot line, purple dot line and the red solid line present the conductances versus the increase of strain. It is clearly shown that along with the increase of strain, the plateaus at $6e^2/h$, $14e^2/h$, $22e^2/h$, $30e^2/h$ become narrower. Until they disappear, the step interval between adjacent plateaus changes from $4e^2/h$ to $8e^2/h$. Meanwhile, P_1 and P_2 appear gradually because of the formations of new edge states.

Next we examine the effect of disorder on the snake states. In the following calculations, we suppose that the disorder only exists in the central region, and in the presence of disorder, we take 500 random configurations and calculate the average values of the conductances. Since this procedure has high computation cost, we cannot take the same number of E_F as that in Fig. 4(b) and (c). However, to avoid missing information related to P_1 and P_2 , we take more number of E_F around them in the calculations. The detailed results are illustrated in Fig. 4(d) and the drawing of partial enlargement of the first plateau, P_1 and P_2 are shown in Fig. 4(e) and (f), respectively. The results can be summarized as follows: (i) when the strength of disorder is very weak, e.g., $w \leq 0.1$ eV, all plateaus, except for P_1 and P_2 , maintain well. P_1 and P_2 are not robust because the range of band structure inside the orange dot rectangle in Fig. 1(e) is small. Moreover, this type of peaks will become more fragile on higher plateaus. (ii) When the strength of disorder increase, e.g., $w = 0.5$ eV, only the first plateau is robust. It is noted that there is a minimum of conductance in the vicinity of $E_F = 0$ in Fig. 4(d) and (e), which may be explained by the Anderson localization [64]. Since the number of propagating channels in the narrow ribbons is very small near $E_F = 0$, the GNR can be viewed as a quasi-1D system. As a result, the conductance dip will appear due to the Anderson localization if the length of the GNR is longer than the localization length. The physical reason why the conductance plateaus is not so robustness is the snake states are easy to become hybrid due to the close distance between them in the real space. Therefore, we need to explore schemes preventing the hybridization and obtain more robust snake states in the middle of the sample.

V. CONCLUSIONS

The valley degree of freedom attributed to the non-equivalent Dirac points K and K' is well-known for decades. Furthermore, strain can be used to tailor the band structures and properties of the ZGNRs, and the most charming phenomenon is the emergent pseudo-magnetic fields and the corresponding pLLs. In order to explore new types of pure valley currents, we design the strained ZGNR which can support the snake states propagating in the middle of the sample. We point out that the reverse strains between the lower and half planes is the essential ingredient for the formation of the snake states. Based on our design, we can use a four-terminal device to realize the long-thought pure valley currents in monolayer graphene systems. Furthermore, we calculate the conductance of the two-terminal device, obtaining the $8e^2/h$ step interval between neighbouring plateaus, which indicates the formation of the snake states in the middle of the sample. By introducing the Anderson impurities, we find that the first conductance plateau is more robust than higher plateaus. One obstacle to the robustness of the snake states is they are easy to become hybrid due to the close distance between them in the real space. One of the next aim is to explore schemes preventing the hybridization and obtain more robust snake states in the middle of the sample.

ACKNOWLEDGMENTS

The authors would like to thank Qing-feng Sun, Shuai Zhao, Chui-zhen Chen and Shu-feng Zhang for helpful discussions. We are grateful to the National Natural Science Foundation of China (Nos. 11774093, 11104075), Science and Technology Commission of Shanghai Municipality (No. 16ZR1409800), Natural Science Foundation of Shanghai (Grant No. 21JC1402300) and Director's Fund of Key Laboratory of Polar Materials and Devices, Ministry of Education.

Appendix A: The value of the pseudo-magnetic field

The value of the pseudo-magnetic field in our model can be estimated by the method used in Ref. [30]. Fig. 5(a) is the band structure adopted from Fig. 1(e). We select several energy points marked by green circles and compare them with the Landau levels generated by the real magnetic fields $E_n = v_F \sqrt{2e\hbar B} \text{sgn}(n) \sqrt{|n|}$, where n is the index of the Landau levels and $v_F \approx 10^6$ m/s is the Fermi velocity. We can read from the slope in Fig. 5(b) that the pseudo-magnetic field $B \approx 49$ T. It should be pointed out according to the relations:

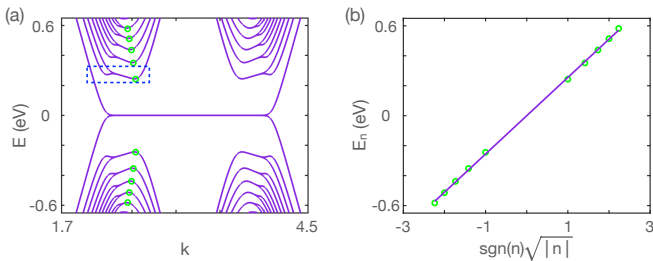


FIG. 5. (a) The band structure adopted from Fig. 1(e). (b) The comparison between the energy points marked by green circles in (a) and the Landau levels generated by the real magnetic field.

$$\begin{aligned}
 A_x &= \frac{c}{2ev_F} (t_2 + t_3 - 2t_1) = \frac{c}{ev_F} (t_0 - t(y)), \\
 A_y &= \frac{\sqrt{3}c}{2ev_F} (t_3 - t_2) = \frac{\sqrt{3}c}{2ev_F} (t_0 - t_0) = 0, \quad (\text{A1})
 \end{aligned}$$

the magnetic field $\mathbf{B} = \nabla \times \mathbf{A}$ is a constant field along the z direction since we have assumed that $t(y)$ is a linear function of y in both upper and lower half planes.

Appendix B: Discussions on P_1 and P_2

Fig. 6(a) is the partial enlarged picture of the bands in the blue dashed box in Fig. 5(a). In order to show

the reason why the extra conductance $2e^2/h$ ($4e^2/h$ if spin is considered) emerges due to P_1 more clearly, we plot the spatial distributions of the eigenstates belong to $E = 0.33$ eV, $E = 0.275$ eV and $E = 0.255$ eV in Figs. 6(b)-(d), respectively. It is clear that P_1 emerges around $E = 0.275$ eV because of the extra intersection points 2B and 2C, which contributes the conductance $2e^2/h$. From Fig. 6(c) we can see that the wave functions of 2B and 2C are localized around the middle region of the sample. The emergence of P_2 can be analysed in the same way.

It should be pointed out that, one of the main difference between the pseudo-Landau levels and the conventional Landau levels is the former are dispersive because of the interaction between the bulk states and edge states. As a result, crossing with the bulk states belonging to the pseudo-Landau levels can always appear when we continuously tune the Fermi energy, e.g., the intersection point 3B in Fig. 6. Furthermore, due to the interaction between the bulk states and edge states, the localization strength of certain states is not that strong. As we know, the robustnesses of the bulk states, edge states and snake states are different, as a result, the stability of the conductance plateaus needs to be studied further.

-
- [1] A. H. C. Neto, F. Guinea, N. M. R. Peres, K. S. Novoselov, and A. K. Geim, The electronic properties of graphene, *Rev. Mod. Phys.* **81**, 109 (2009).
 - [2] A. Rycerz, J. Tworzydło and C. W. J. Beenakker, Valley filter and valley valve in graphene, *Nat. Phys.* **3**, 172 (2007).
 - [3] D. Xiao, W. Yao, and Q. Niu, Valley-contrasting physics in graphene: magnetic moment and topological transport, *Phys. Rev. Lett.* **99**, 236809 (2007).
 - [4] J. R. Schaibley, H. Yu, G. Clark, P. Rivera, J. S. Ross, K. L. Seyler, W. Yao, and X. Xu, Valleytronics in 2D materials, *Nat. Rev. Mater.* **1**, 16055 (2016).
 - [5] Y. D. Lensky, J. C. W. Song, P. Samutpraphoot, and L. S. Levitov, Topological valley currents in gapped Dirac materials, *Phys. Rev. Lett.* **114**, 256601 (2015).
 - [6] D. Xiao, G.-B. Liu, W. Feng, X. Xu, and W. Yao, Coupled spin and valley physics in monolayers of MoS₂ and other group-VI dichalcogenides, *Phys. Rev. Lett.* **108**, 196802 (2012).
 - [7] K. Chang, B. J. Miller, H. Yang, H. Lin, S. S. P. Parkin, S. Barraza-Lopez, Q.-K. Xue, X. Chen, and S.-H. Ji, *Phys. Rev. Lett.* **122**, 206402 (2019).
 - [8] R.-J. Slager, V. Juričić, V. Lahtinen, and J. Zaanen, Self-organized pseudo-graphene on grain boundaries in topological band insulators, *Phys. Rev. B* **93**, 245406 (2016).
 - [9] K. Nakada, M. Fujita, G. Dresselhaus, and M. S. Dresselhaus, Edge state in graphene ribbons: Nanometer size effect and edge shape dependence, *Phys. Rev. B* **54**, 17954 (1996).
 - [10] S. Wang, L. Talirz, C. A. Pignedoli, X. Feng, K. Müllen, R. Fasel, and P. Ruffieux, Giant edge state splitting at atomically precise graphene zigzag edges, *Nat. Commun.* **7**, 11507 (2016).
 - [11] Z.-q. Bao, J.-j. Shi, and M. Zhang, Ferromagnetism, adatom effect, and edge reconstruction induced by Klein boundary in graphene nanoribbons, *J. Appl. Phys.* **113**, 194302 (2013).
 - [12] T.-l. Lu, C.-y. Zuo, M. Zhang, Z.-q. Bao, and Y. Li, Magnetic localized states and tunable magnetism of single vacancies in generalized chiral graphene nanoribbons, *Mater. Res. Express* **8**, 045602 (2021).
 - [13] J.-W. Rhim, J. H. Bardarson, and R.-J. Slager, Unified bulk-boundary correspondence for band insulators, *Phys. Rev. B* **97**, 115143 (2018).
 - [14] V. Atanasov and A. Saxena, Electronic properties of corrugated graphene: the Heisenberg principle and worm-hole geometry in the solid state, *J. Phys. Condens. Matter* **23**, 175301 (2011).
 - [15] K. Roy, S. Bandyopadhyay, and J. Atulasimha, Hybrid spintronics and straintronics: A magnetic technology for ultra low energy computing and signal processing, *J*

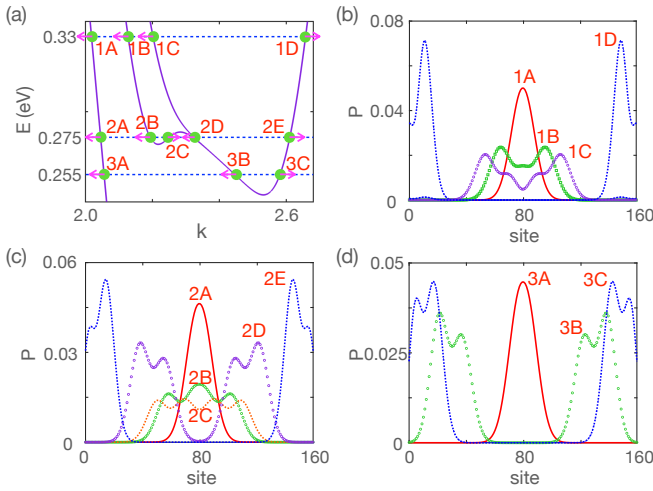


FIG. 6. Spatial distributions of the eigenstates belong to $E = 0.33$ eV, $E = 0.275$ eV and $E = 0.255$ eV, respectively.

- Appl. Phys. Lett.* **99**, 063108 (2011).
- [16] A. A. Bukharaev, A. K. Zvezdin, A. P. Pyatakov, and Y. K. Fetisov, Straintronics: a new trend in micro- and nanoelectronics and materials science, *Phys.-Usp.* **61**, 1175 (2018).
- [17] J. Sun, H. Guo, and S. Feng, Magnon Landau levels in the strained antiferromagnetic honeycomb nanoribbons, *Phys. Rev. Research* **3**, 043223 (2021).
- [18] B. Roy, Z.-X. Hu, and K. Yang, Theory of unconventional quantum Hall effect in strained graphene, *Phys. Rev. B* **87**, 121408(R) (2013).
- [19] S. G. Stuij, P. H. Jacobse, V. Juričić, and C. M. Smith, Tuning edge state localization in graphene nanoribbons by in-plane bending, *Phys. Rev. B* **92**, 075424 (2015).
- [20] E. Cadelano, P. L. Palla, S. Giordano, and L. Colombo, Nonlinear elasticity of monolayer graphene, *Phys. Rev. Lett.* **102**, 235502 (2009).
- [21] C. Lee, X. Wei, J. W. Kysar, and J. Hone, Measurement of the elastic properties and intrinsic strength of monolayer graphene, *Science* **321**, 385 (2008).
- [22] F. Liu, P. Ming, and J. Li, Ab initio calculation of ideal strength and phonon instability of graphene under tension, *Phys. Rev. B* **76**, 064120 (2007).
- [23] I. Yu. Sahalianov, T. M. Radchenko, V. A. Tatarsenko, G. Cuniberti, and Y. I. Prylutskyy, Straintronics in graphene: Extra large electronic band gap induced by tensile and shear strains, *J. Appl. Phys.* **126**, 054302 (2019).
- [24] V. M. Pereira, A. H. Castro Neto, and N. M. R. Peres, Tight-binding approach to uniaxial strain in graphene, *Phys. Rev. B* **80**, 045401 (2009).
- [25] J. L. Mañes, Symmetry-based approach to electron-phonon interactions in graphene, *Phys. Rev. B* **76**, 045430 (2007).
- [26] F. Guinea, M. I. Katsnelson, and A. K. Geim, Energy gaps and a zero-field quantum Hall effect in graphene by strain engineering, *Nat. Phys.* **6**, 30 (2010).
- [27] T. Low and F. Guinea, Strain-induced pseudomagnetic field for novel graphene electronics, *Nano Lett.* **10** 3551 (2010).
- [28] M. A. H. Vozmediano, M. I. Katsnelson, and F. Guinea, Gauge fields in graphene, *Phys. Rep.* **496**, 109 (2010).
- [29] F. de Juan, J. L. Mañes, and María A. H. Vozmediano, Gauge fields from strain in graphene, *Phys. Rev. B* **87**, 165131 (2013).
- [30] W.-Y. He and L. He, Coupled spin and pseudomagnetic field in graphene nanoribbons, *Phys. Rev. B* **88**, 085411 (2013).
- [31] S. Zhu, J. A. Stroscio, and T. Li, Programmable extreme pseudomagnetic fields in graphene by a uniaxial stretch, *Phys. Rev. Lett.* **115**, 245501 (2015).
- [32] M. Settnes, S. R. Power, and A.-P. Jauho, Pseudomagnetic fields and triaxial strain in graphene, *Phys. Rev. B* **93**, 035456 (2016).
- [33] D. Sabsovich, M. W. Bockrath, K. Shtengel, and E. Sela, Helical superconducting edge modes from pseudo-Landau levels in graphene, *Phys. Rev. B* **103**, 094513 (2021).
- [34] N. Levy, S. A. Burke, K. L. Meaker, M. Panlasigui, A. Zettl, F. Guinea, A. H. C. Neto, and M. F. Crommie, Strain-induced pseudo-magnetic fields greater than 300 tesla in graphene nanobubbles, *Science* **329**, 544 (2010).
- [35] J. Lu, A. H. Castro Neto, and K. P. Loh, Transforming moiré blisters into geometric graphene nano-bubbles, *Nat. Commun.* **3**, 823 (2012).
- [36] S.-Y. Li, K.-K. Bai, L.-J. Yin, J.-B. Qiao, W.-X. Wang, and L. He, Observation of unconventional splitting of Landau levels in strained graphene, *Phys. Rev. B* **92**, 245302 (2015).
- [37] Y. Liu, J. N. B. Rodrigues, Y. Z. Luo, L. Li, A. Carvalho, M. Yang, E. Laksono, J. Lu, Y. Bao, H. Xu, S. J. R. Tan, Z. Qiu, C. H. Sow, Y. P. Feng, A. H. C. Neto, S. Adam, J. Lu, and K. P. Loh, Tailoring sample-wide pseudo-magnetic fields on a graphene-black phosphorus heterostructure, *Nat. Nanotechnology* **13**, 828 (2018).
- [38] P. Nigge, A. C. Qu, É. Lantagne-Hurtubise, E. Mårsell, S. Link, G. Tom, M. Zonno, M. Michiardi, M. Schneider, S. Zhdanovich, G. Levy, U. Starke, C. Gutiérrez, D. Bonn, S. A. Burke, M. Franz, and A. Damascelli, Room temperature strain-induced Landau levels in graphene on a wafer-scale platform, *Sci. Adv.* **5**, eaaw5593 (2019).
- [39] S.-Y. Li, Y. Su, Y.-N. Ren, and L. He, Valley polarization and inversion in strained graphene via pseudo-Landau levels, valley splitting of real Landau levels, and confined states, *Phys. Rev. Lett.* **124**, 106802 (2020).
- [40] Étienne Lantagne-Hurtubise, X.-X. Zhang, and M. Franz, Dispersive Landau levels and valley currents in strained graphene nanoribbons, *Phys. Rev. B* **101**, 085423 (2020).
- [41] E. Sela, Y. Bloch, F. von Oppen, and M. B. Shalom, Quantum Hall response to time-dependent strain gradients in graphene, *Phys. Rev. Lett.* **124**, 026602 (2020).
- [42] N. N. Klimov, S. Jung, S. Zhu, T. Li, C. A. Wright, S. D. Solares, D. B. Newell, N. B. Zhitenev, and J. A. Stroscio, Electromechanical properties of graphene drumheads, *Science* **336**, 1557 (2012).
- [43] J. C. Meyer, A. K. Geim, M. I. Katsnelson, K. S. Novoselov, T. J. Booth, and S. Roth, The structure of suspended graphene sheets, *Nature* **446**, 60 (2007).
- [44] S. Zhu, Y. Huang, N. N. Klimov, D. B. Newell, N. B. Zhitenev, J. A. Stroscio, S. D. Solares, and T. Li, Pseudomagnetic fields in a locally strained graphene drumhead, *Phys. Rev. B* **90**, 075426 (2014).

- [45] W. Long, Q.-f. Sun, and J. Wang, Disorder-induced enhancement of transport through graphene p - n junctions, *Phys. Rev. Lett.* **101**, 166806 (2008).
- [46] J. L. Lado, J. W. González, and J. Fernández-Rossier, Quantum Hall effect in gapped graphene heterojunctions, *Phys. Rev. B* **88**, 035448 (2013).
- [47] J. Amasay and E. Sela, Transport through dynamic pseudogauge fields and snake states in a Corbino geometry, *Phys. Rev. B* **104**, 125428 (2021).
- [48] T. K. Ghosh, A. De Martino, W. Häusler, L. Dell'Anna, and R. Egger, Conductance quantization and snake states in graphene magnetic waveguides, *Phys. Rev. B* **77**, 081404(R) (2008).
- [49] L. Oroszlány, P. Rakytá, A. Kormányos, C. J. Lambert, and J. Cserti, Theory of snake states in graphene, *Phys. Rev. B* **77**, 081403(R) (2008).
- [50] G. W. Jones, D. A. Bahamon, A. H. Castro Neto, and V. M. Pereira, Quantized transport, strain-induced perfectly conducting modes, and valley filtering on shape-optimized graphene corbino devices, *Nano Lett.* **17**, 5304 (2017).
- [51] L. E. Golub, S. A. Tarasenko, M. V. Entin, and L. I. Margarill, Valley separation in graphene by polarized light, *Phys. Rev. B* **84**, 195408 (2011).
- [52] J. Wang, K. S. Chan, and Z. Lin, Quantum pumping of valley current in strain engineered graphene, *Appl. Phys. Lett.* **104**, 013105 (2014).
- [53] J. Wang, Z. Lin and K. S. Chan, Pure valley current generation in graphene with a Dirac gap by quantum pumping, *Appl. Phys. Express* **7**, 125102 (2014).
- [54] Y. Jiang, T. Low, K. Chang, M. I. Katsnelson, and F. Guinea, Generation of pure bulk valley current in Graphene, *Phys. Rev. Lett.* **110**, 046601 (2013).
- [55] H. Yu, Y. Wu, G.-B. Liu, X. Xu, and W. Yao, Nonlinear valley and spin currents from Fermi pocket anisotropy in 2D crystals, *Phys. Rev. Lett.* **113**, 156603 (2014).
- [56] R. V. Gorbachev, J. C. W. Song, G. L. Yu, A. V. Kretinin, F. Withers, Y. Cao, A. Mishchenko, I. V. Grigorieva, K. S. Novoselov, L. S. Levitov, and A. K. Geim, Detecting topological currents in graphene superlattices, *Science* **346**, 448 (2014).
- [57] M. Sui, G. Chen, L. Ma, W.-Y. Shan, D. Tian, K. Watanabe, T. Taniguchi, X. Jin, W. Yao, D. Xiao, and Y. Zhang, Gate-tunable topological valley transport in bilayer graphene, *Nat. Phys.* **11**, 1027 (2015).
- [58] Y. Shimazaki, M. Yamamoto, I. V. Borzenets, K. Watanabe, T. Taniguchi, and S. Tarucha, Generation and detection of pure valley current by electrically induced Berry curvature in bilayer graphene, *Nat. Phys.* **11**, 1032 (2015).
- [59] J. Li, R.-X. Zhang, Z. Yin, J. Zhang, K. Watanabe, T. Taniguchi, C. Liu, and J. Zhu, A valley valve and electron beam splitter, *Science* **362**, 1149 (2018).
- [60] S. K. FirozIslam and C. Benjamin, A scheme to realize the quantum spin-valley Hall effect in monolayer graphene, *Carbon* **110**, 304 (2016).
- [61] C. L. Kane and E. J. Mele, Quantum spin Hall effect in graphene, *Phys. Rev. Lett.* **95**, 226801 (2005).
- [62] M. Büttiker, Four-terminal phase-coherent conductance, *Phys. Rev. Lett.* **57**, 1761 (1986).
- [63] W. Ren, Z. Qiao, J. Wang, Q.-f. Sun, and H. Guo, Universal spin-Hall conductance fluctuations in two dimensions, *Phys. Rev. Lett.* **97**, 066603 (2006).
- [64] E. R. Mucciolo, A. H. Castro Neto, and C. H. Lewenkopf, Conductance quantization and transport gaps in disordered graphene nanoribbons, *Phys. Rev. B* **79**, 075407 (2009).